

## Effect on measurements of anemometers due to a passing high-speed train

Jie Zhang<sup>a</sup>, Guangjun Gao<sup>b</sup>, Sha Huang<sup>c</sup> and Tanghong Liu<sup>\*</sup>

Key Laboratory of Traffic Safety on Track of Ministry of Education, School of Traffic & Transportation Engineering, Central South University, Changsha 410075, Hunan, China

(Received July 3, 2014, Revised February 9, 2015, Accepted February 10, 2015)

**Abstract.** The three-dimensional unsteady incompressible Reynolds-averaged Navier-Stokes equations and  $k-\varepsilon$  double equations turbulent model were used to investigate the effect on the measurements of anemometers due to a passing high-speed train. Sliding mesh technology in Fluent was utilized to treat the moving boundary problem. The high-speed train considered in this paper was with bogies and inter-carriage gaps. Combined with the results of the wind tunnel test in a published paper, the accuracy of the present numerical method was validated to be used for further study. In addition, the difference of slipstream between three-car and eight-car grouping models was analyzed, and a series of numerical simulations were carried out to study the influences of the anemometer heights, the train speeds, the crosswind speeds and the directions of the induced slipstream on the measurements of the anemometers. The results show that the influence factors of the train-induced slipstream are the passing head car and tail car. Using the three-car grouping model to analyze the train-induced flow is reasonable. The maxima of horizontal slipstream velocity tend to reduce as the height of the anemometer increases. With the train speed increasing, the relationship between  $V_{\text{train}}$  and  $V_{\text{induced slipstream}}$  can be expressed with linear increment. In the absence of natural wind conditions, from the head car arriving to the tail car leaving, the induced wind direction changes about  $330^\circ$ , while under the crosswind condition the wind direction fluctuates around  $-90^\circ$ . With the crosswind speed increasing, the peaks of  $V_x$ ,  $|V_{xy} - V_{\text{wind}}|$  of the head car and that of  $V_x$  of the tail car tend to enlarge. Thus, when anemometers are installed along high-speed railways, it is important to study the effect on the measurements of anemometers due to the train-induced slipstream.

**Keywords:** train-induced slipstream; anemometer; crosswind; direction; numerical simulation

### 1. Introduction

The landform environment along railway lines in China is complex and varied due to its vast territory, especially in the second channel from Lanchow to Urumqi and the coastal passenger lines, where the railway lines are exposed to strong winds (typhoon) throughout the year. In order to ensure the operational safety of high-speed trains, it is necessary to set up anemology stations to

---

\*Corresponding author, Associate Professor, E-mail: lthjd@163.com

<sup>a</sup> Ph.D. Student, E-mail: jie\_csu@csu.edu.cn

<sup>b</sup> Professor, E-mail: gjgao@csu.edu.cn

<sup>c</sup> Ph.D. Student, E-mail: joanna\_119@163.com

monitor the wind speed and direction changes along the railway lines in windy areas, which is a significant part of the strong wind warning system. Thus the measurement accuracy and layout of the anemology stations directly affect the transportation efficiency and the train operation safety.

However, due to the existence of the viscous effect, the air around a train will move at a certain speed as the train body moves forward, forming instantaneous slipstreams that may affect the measurement of anemometers. When the train runs at low speed, the effect of the slipstream flow is less turbulent and has small peaks that can be ignored. However, as the train speed increases, the turbulence intensity increases and the slipstream peaks rise up, which may pose a safety risk to track infrastructures (Sanz-Andres *et al.* 2002), passengers and trackside workers (Baker *et al.* 2006, Sterling *et al.* 2008). Hence the need for measurement instruments such as sensors along the railway line. In the gale region, in order to guarantee the operational safety of trains, anemometers are widely used along the high-speed railway (Fujii *et al.* 1999, Matsumoto *et al.* 1996, Gong and Wang 2012). To find out the extent of the effect on the measurements of anemometers due to passing high-speed trains, much work has to be carried out.

Recently, concerning the induced slipstream, scholars at home and abroad have conducted related research and some studies have been published on the pressure/loads induced by a vehicle/train on pedestrians (Baker *et al.* 2006, Sanz-Andres *et al.* 2002 and 2004, Hur *et al.* 2008, Huang *et al.* 2014), vehicle-induced forces on flat plates (Juraeva *et al.* 2011, Quinn *et al.* 2001a,b, Sanz-Andres *et al.* 2004) and sign structures (Sanz-Andres *et al.* 2003, Philip *et al.* 2000), vehicle-induced loads on insulated boards (Li and Liang 2009), and so on. Based on the theoretical models, some investigations have been made to explain the time variation of the loads/forces and pressure. However, the case of the slipstream velocity effect on a measurement instrument is seldom considered. There is a lack of studies about the effect on this along the railway, especially on anemometers, although their measurement data directly affect the transportation efficiency.

In this paper, the three-dimensional unsteady Reynolds-averaged Navier–Stokes equations (RANS) combined with the eddy viscosity hypothesis model were adopted to obtain the horizontal wind speed generated by the head and tail of a passing train, and the dependence with the moving distance of the wind generated at the anemometer point. The validity of the model developed here is verified with the wind tunnel test.

On the basis of the former theoretical and experimental researches, it is found that the main parameters that influence the induced wind velocity are the train speed, the vehicle cross-section area, and the distance between the object and the train. Of course, the head shape of the train is also important. However, a streamlined head has been used in a wide range of applications, so in this paper a common kind of high-speed train in China that consists of three coaches or eight coaches is considered. The slipstream flow around the train was first calculated. Then the effects of the height of the anemometer point and the speed of the train were then both further analyzed. Based on these, the effects of the horizontal wind velocity and direction acting on the anemometer point were obtained, which can provide guidance for the measurement and location of anemometers along railway lines.

## 2 Computational details

### 2.1 Mathematical model

For high-speed trains operating in China, the maximum running speed is 350 km/h, making the

Mach number less than 0.3, so the aerodynamic issues of high-speed trains in open air can be considered as incompressible flow. Then the commercial CFD software Fluent was used, and the three-dimensional unsteady Reynolds-averaged Navier–Stokes equations (RANS) (Fluent Inc 2006, Tian 2007, Wang *et al.* 2014) and  $k-\varepsilon$  double equations turbulent model (Li and Liang 2009, Zhang *et al.* 2013, Liu and Zhang 2013) are utilized to compute the flow field. The computational domain was discretized by the Finite Volume Method (FVM). Simulations were performed using a pressure-based solver. The Navier–Stokes equations were solved using the second-order upwind scheme. The time derivative was discretized using the first-order implicit scheme for unsteady flow calculation. In numerical simulations, the algorithm used for pressure-velocity field coupling was SIMPLEC (Semi-Implicit Method for Pressure-Linked Equations-Consistent). The convergence criterion of the continuity equation was  $10^{-4}$ .

## 2.2 Sliding mesh technology

To account for the relative motion between the stationary ground and moving train, sliding mesh technology (Shin *et al.* 2003, Tian 2007, Li and Liang 2009, Juraeva *et al.* 2011, Shu *et al.* 2014) was utilized. The computational zone is divided into two regions, as shown in Fig. 1. Region 1 concludes train and the space around it, and Region 2 is for the region with anemometer points and their surroundings far away from the train. In addition, a grid interface is used to describe the interface information of two regions. During the simulation, the two independent regions (Region 1 and Region 2) can move relative to one another along the train length direction without mesh regeneration, which is the main difference from dynamic mesh technology (Fluent Inc 2006). To use sliding mesh technology, a method with which to compute the fluxes across each grid point inside the non-conformal interfaces is required, and the information exchange of fluid field can be shown in Fig. 2. In order to transfer the flow field information from one region to one another, at every time step, the intersection grids (such as the grid points:  $b, c, d, \dots, h$  in Fig. 2) between the interfaces are determined by the interfaces of Region 1 and Region 2 with a segmentation of each other to form a common face  $a-b-c-d-e-f-g-h-i$ . As the regions move relative to one another, the number of intersection grids will change. The fluxes across the grid interface are computed using intersection grids rather than the grids on each interface. For example, the interfaces are composed of face  $A-B-C-D-E$  and face  $F-G-H-I$  in Fig. 2. To compute the flux across the interface and bring information from Cells II and III into Cell VI, face  $d-e-f$  is used, instead of face  $G-H$ . Therefore, the fluid field information can be communicated between two adjacent regions.

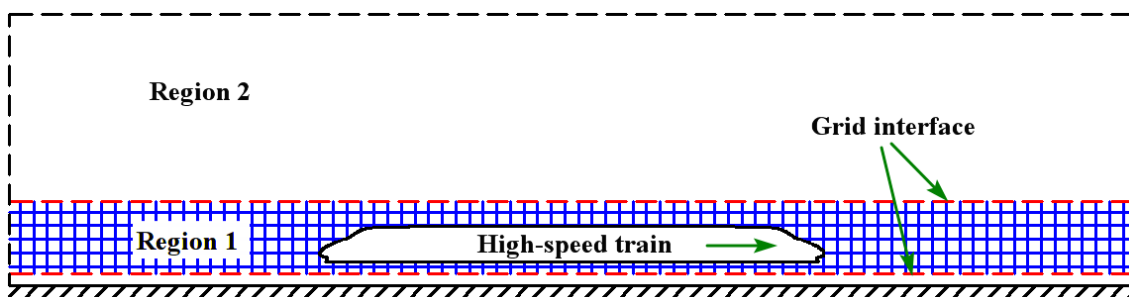


Fig. 1 Regions of sliding mesh technology

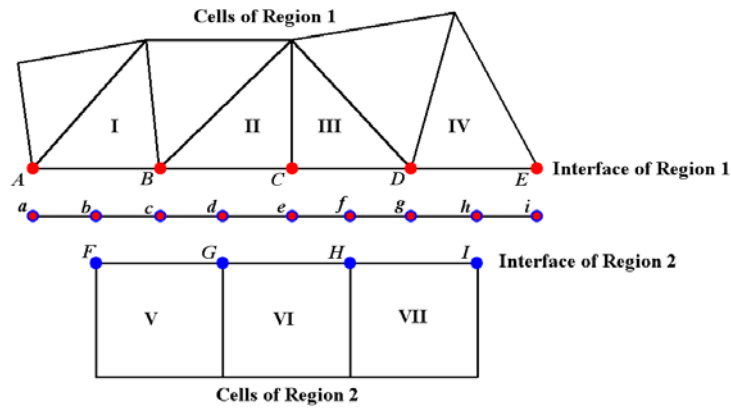


Fig. 2 Schematic diagram of sliding mesh technology

### 2.3 Computational domain, boundary condition and computational grid

A simplified high-speed train model formed of three coaches was used, as shown in Fig. 3. The total length is 76.4 m with a length to width to height ratio of 1: 0.04424: 0.04843. In addition, the eight-car grouping model, which just added 5 middle coaches to the three-car grouping model, was used for comparison. For the computations, the geometry structure was smoothed, having bogies underneath and inter-carriage gaps covered by semi-closed windshields.

The computational domain is illustrated in Fig. 4. The height of the train model is defined as the characteristic dimension, denoted by  $h$ .

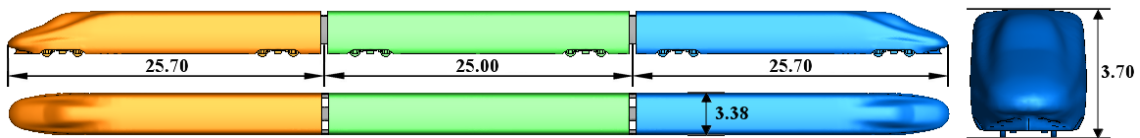


Fig. 3 High-speed train model

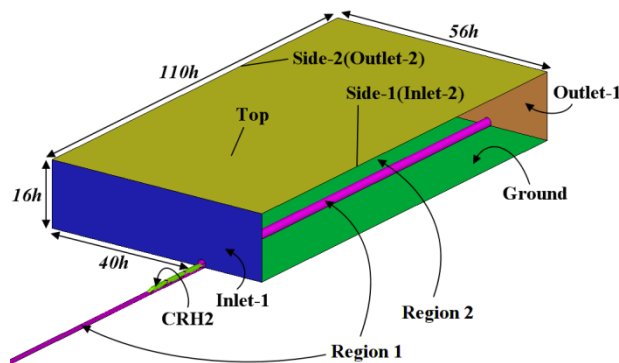


Fig. 4 Computational domain

First, the boundary condition was set as the stationary condition, and the train was located  $27h$  (100 m) away from the anemometer point. Fig. 5 shows the installation position of the anemometer point. Along high-speed railways, the height of anemometer point R1 above rail level is always 4 m. Point R4 is a symmetry point relative to point R1. Points R2 and R3 are just reference ones to analyze point R1. The heights are 3 m and 5 m, respectively. All these points are located in Region 2, which is motionless. Then the train moved at a constant speed. The ground was treated as a non-slip wall. When the train moved, Region 1 entered into Region 2. Inlet-1 was set to be the Pressure-Inlet, while Outlet-1 was the Pressure-Outlet. Under the no crosswind condition, the two sides of the computational domain were treated as a symmetry boundary, while these were specified as Velocity-Inlet and Pressure-Outlet under the crosswind condition, respectively. The computational domain was discretized using structured and unstructured hybrid grids. Triangular grids were used for the body surfaces of the train, and tetrahedral grids for the volume around the train. Moreover, all were structured grids. As to the numerical predictions, the grids that were near the body surfaces of the train were refined. Fig. 6 shows the computational mesh.

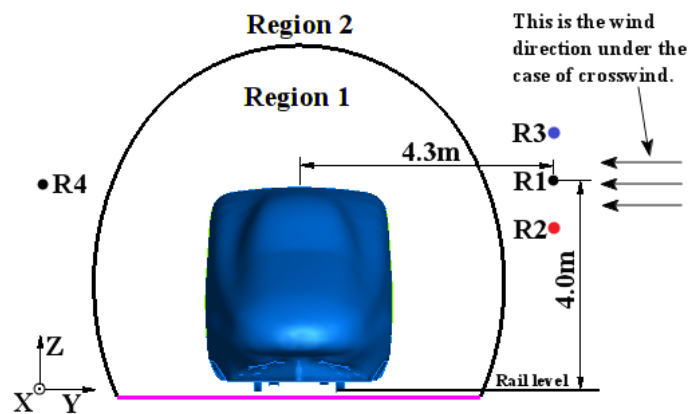


Fig. 5 Sketch map of anemometer points

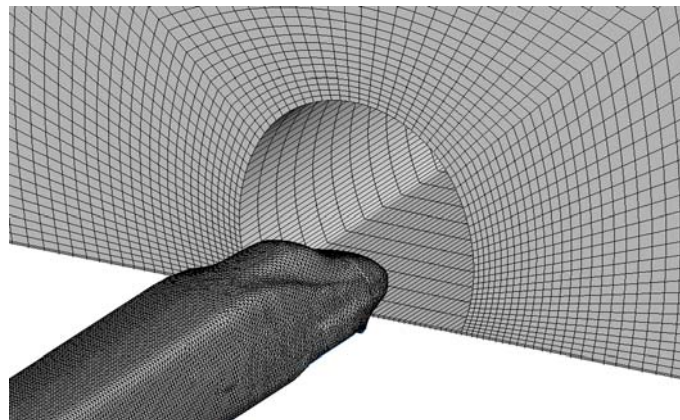


Fig. 6 Computational mesh

### 3. Results and discussion

#### 3.1 Program validation

To validate the accuracy of the present numerical method, the data in this paper will be compared with the experimental data in the publication by Zhang *et al.* (2013), which has been converted into the results at full scale. In this test, a three-car grouping model is 1/15<sup>th</sup> scale, the same as the one for simulation, positioned on a flat ground. The synthetic wind speed is 60 m/s. The wind direction is chosen as the angle 10° according to the yaw angle  $\beta$  (Liu and Zhang 2013), which is 10.2° between the current train speed (300 km/h) and wind velocity (15 m/s). According to the publications by Hemida and Krajnovic (2010b), Hemida *et al.* (2014) and Tian (2007), when the simulations are performed at a Reynolds number of 300,000 and above, the flow is fully turbulent and hence the non-dimension coefficients of aerodynamic forces are believed to be Reynolds numbers independent at the same wind direction. Then the non-dimension coefficients of the overturning moment can be defined as follows:  $C_M = M / (qhA)$  (Zhang *et al.* 2013, Diedrichs *et al.* 2007, Cheli *et al.* 2010, Rezvani and Mohebbi 2014), where  $q = 0.5\rho(V_{\text{train}}^2 + V_{\text{wind}}^2)$ ,  $q$  is the dynamic pressure,  $V_{\text{train}}$  is the speed of the train, and  $V_{\text{wind}}$  is the wind speed,  $M$  is the overturning moment,  $A$  is the reference area which is 10 m<sup>2</sup> in this analysis,  $h$  is the height of the train, and  $\rho$  is the constant air density that is 1.225 kg/m<sup>3</sup>. Table 1 shows the validation results in this program.

Comparing the experimental and simulation results, the table presents a reasonable agreement. For the tail car, there is a slight larger difference between the test and simulation results. The aerodynamic force of the tail car is the least in all the cars, and takes up less than 14% of that of the train-set in the wind tunnel test in the publication by Zhang *et al.* (2013). In addition, according to Huang's research (2014), when the monitoring point is at a distance of over 2.18 m from the center line of the nearer track and 3.8 m above the rail level, the effect of the wake flow will be very weak. At this time, the slipstream velocities are dependant on the train heads passing, including the the curved surfaces of the head car and the tail car. The anemometer points in this paper are at a distance of 4.3 m from the center line of the nearer track, therefore, it indicates that the present numerical method can be used for further study.

#### 3.2 Comparison between three-car and eight-car grouping models

In China, high-speed trains are always eight-car or sixteen-car groupings. In order to prove the three-car grouping model in this paper to be suitable, a comparison has been made between the two grouping models. The train speed is 300 km/h. The Reynolds number is  $2.1 \times 10^7$ , based on the train speed and the train height. Fig. 7 shows the comparison of the effect on anemometer points due to the train-induced slipstream between the three-car and eight-car grouping models. Only point R1 is considered.

Table 1 Comparison between experimental and simulation results for  $C_M$  at a full-scale model

Method	$C_{M\text{-head}}$	$C_{M\text{-middle}}$	$C_{M\text{-tail}}$
Wind tunnel test	-0.5021	-0.2853	-0.1255
Numerical simulation	-0.4852	-0.2877	-0.0993
Absolute value of error	3.37%	0.84%	20.88%

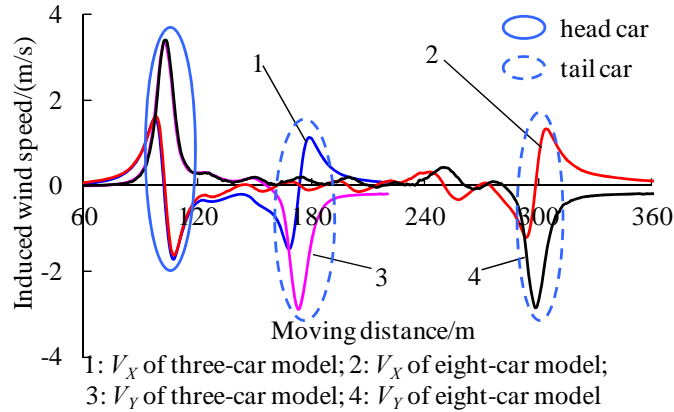


Fig. 7 Comparison of the effect on point R1 between two models

Through the analysis of this figure, it can be seen that the influence factors of train-induced slipstream velocity are the passing head car and tail car, particularly the head. When the middle cars are passing the anemometer point, they merely cause a slight disturbance of the slipstream, and the effect is much less than that of the head and tail cars. With either the three-car or eight-car grouping, the wind speed variations of the slipstream are almost the same as the head car passes. In the X axis direction, as the moving distance increases, the speed rises sharply to the peak at the time of the head car arriving. Then it reduces suddenly to the negative extremum. The maximum, without consideration of the vector direction, based on the three-car grouping, reaches 1.70 m/s, while the eight-car grouping reaches 1.63 m/s. At the same time, in the Y axis direction, the wind speed increases rapidly to the peak at the time of the head car passing. Subsequently, it drops to near 0. The maximum reaches 3.38 m/s, 3.39 m/s, respectively. However, the time of the peak of  $V_X$  is not the same as that of  $V_Y$ . The former is faster, and at the time it reduces to 0, the latter just reaches the peak. As the tail car is passing the anemometer point, the result is similar to that of the head car, but the change law is opposite. Due to the different number of middle cars, the times of the maximum are not equal. These data present reasonable agreements. While anemometers along the railway line are often used to measure the horizontal wind velocity, including  $V_X$ ,  $V_Y$  and  $V_{XY}$ , that of the Z axis isn't taken into account. Thus, using the three-car grouping model to analyze the train-induced flow is reasonable.

### 3.3 Under the case without crosswind

#### 3.3.1 Effect of different heights of anemometers

Based on the analysis above, the main factors affecting the anemometer measurements due to train-induced slipstream are the head car and tail car. Therefore, in the practical application, no matter how long each running train set is, the key time is the time when the head car and tail car are passing. In this section, we investigate the peak value of the slipstream effect at different heights of anemometers. The results are demonstrated in Table 2. Pr is point R4 whose height is also 4 m as a reference point for point R1 in Fig. 5.

Table 2 Peak values of the slipstream effect at different heights of anemometers

$H/m$	Head car			Tail car		
	$V_X/(m/s)$	$V_Y/(m/s)$	$V_{XY}/(m/s)$	$V_X/(m/s)$	$V_Y/(m/s)$	$V_{XY}/(m/s)$
3	1.98	4.48	4.48	1.60	3.57	3.58
4	1.70	3.38	3.40	1.47	2.88	2.90
5	1.48	2.69	2.70	1.32	2.36	2.40
4(Pr)	1.69	3.32	3.33	1.40	2.80	2.81
Specific value						
$V_{3m}/V_{4m}$	1.16	1.33	1.32	1.09	1.24	1.23
$V_{4m}/V_{5m}$	1.15	1.26	1.26	1.11	1.22	1.21
$V_{4m}/V_{Pr}$	1.01	1.02	1.02	1.05	1.03	1.03

The data in Table 2 suggest that as the height of the anemometer increases, the peaks of  $V_X$ ,  $V_Y$  and  $V_{XY}$  tend to reduce and the slipstream effect on the anemometer weakens. The value of  $V_{XY}$  is equal to that of  $V_Y$ , which is nearly twice that of  $V_X$ . All these indicate that  $V_{XY}$  is more dependent on  $V_Y$ . When the head car is passing, the speed peak is larger (Johnson and Holding 2003). Through comparison of the specific values, the ratio of  $V_{3m}/V_{4m}$  is similar to that of  $V_{4m}/V_{5m}$ . However, the values of  $V_X$  are smaller than those of  $V_Y$ , which indicates that the influence of the height of anemometers along the Y axis is more obvious. At the same time, the value of  $V_{4m}/V_{Pr}$  is close to 1, and the maximal error is only 5%. So the effect of the train-induced slipstream is a symmetrical distribution with respect to the trajectory of the center position of the moving train. The relationship between  $H$  and  $V$  ( $V_X$ ,  $V_Y$  and  $V_{XY}$ ) can be expressed in linear form and the correlation coefficients are over 0.99. The following formula can be established:

$$V_{ij} = aH + b$$

where  $j = V_X, V_Y, V_{XY}$ ,  $i = \text{head car, tail car}$ , and the specific coefficients of  $a, b$  are listed in Table 3.

Fig. 8 shows the contrast analysis of the induced wind speeds at points R1 and R4 with distance at the height of 4 m. The  $V_X$  and  $V_{XY}$  values are almost the same.

Table 3 Fitting coefficients of slipstream velocities at different heights

Coefficients	Head car			Tail car		
	$V_X$	$V_Y$	$V_{XY}$	$V_X$	$V_Y$	$V_{XY}$
$a$	-0.250	-0.895	-0.890	-0.140	-0.605	-0.590
$b$	2.720	7.097	7.087	2.023	5.357	5.320

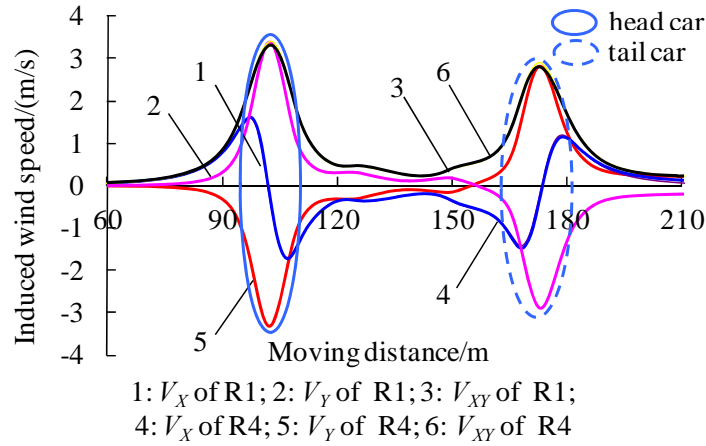


Fig. 8 X, Y, XY component of slipstream velocities at points R1 and R4

From the curves, it is not easy to distinguish which is R1 and which is R4. They further indicate that the train-induced flow is symmetrical in the absence of natural wind conditions. The variations of  $V_Y$ , due to the reverse coordinate direction, are symmetrical related to the distance axis in Fig. 8. The curve of  $V_X$  is a little ahead of the other two, for it is the direction of train movement and the slipstream around the train already has a certain speed. Therefore, the result is that  $V_{XY}$  is more dependent on  $V_Y$ . Meanwhile, the absolute extrema of both are nearly equal.

### 3.3.2 Effect of different train speeds

The train speed varies from 250 km/h to 350 km/h on the high-speed railway. At low speed, the train-induced slipstream velocity is small, but it will become more serious with increasing speed. So it is worthy of investigation. The following mainly concentrates on the effect of different train speeds on the peak value of the slipstream of anemometers.  $V_{train}$  is chosen as 250 km/h, 300 km/h and 350 km/h. The height of point R1 above rail level is 4 m. In this part, the research investigates both cars passing, the head and tail car. The results are shown in Table 4.

Table 4 Peak values of the slipstream effect on point R1 at different train speeds

$V_{train}/$ (km/h)	Head car			Tail car		
	$V_X/(m/s)$	$V_Y/(m/s)$	$V_{XY}/(m/s)$	$V_X/(m/s)$	$V_Y/(m/s)$	$V_{XY}/(m/s)$
250	1.42	2.81	2.82	1.22	2.40	2.42
300	1.70	3.38	3.40	1.47	2.88	2.90
350	1.99	3.94	3.95	1.71	3.37	3.39
Specific value						
$V_{300}/V_{250}$	1.20	1.20	1.21	1.20	1.20	1.20
$V_{350}/V_{300}$	1.17	1.16	1.16	1.16	1.17	1.17

With the train speed increasing, the peaks of  $V_X$ ,  $V_Y$  and  $V_{XY}$  also become larger. The effect of the induced slipstream on the anemometer will strengthen. Still, the value of  $V_{XY}$  is equal to that of  $V_Y$ , which is mainly twice that of  $V_X$ . Through the comparison of the specific values, under the  $V_{300}/V_{250}$  condition, the X, Y and XY components are all near to 1.20, while under the  $V_{350}/V_{300}$  condition, they are 1.16–1.17. All these show that the train speed has a direct effect on the velocity of the anemometer. The slipstream velocity  $V$  ( $V_X$ ,  $V_Y$  and  $V_{XY}$ ) is linearly proportional to the speed of the train  $V_{\text{train}}$ , which presents a reasonable agreement with the research achievement of Professor Tian in her book, *Train Aerodynamics* (Tian 2007), and the publication by Hassan *et al.* (2010a). In addition, the correlation coefficients are over 0.99. Therefore, the following formula can be established:

$$V_{ij} = aV_{\text{train}} + b$$

where  $j = V_X, V_Y, V_{XY}$ ,  $i = \text{head car, tail car}$ , and the specific coefficients of  $a, b$  are listed in Table 5.

Fig. 9 is the contrast analysis of induced wind speed at points R1 and R4 with distance at the height of 4m under different train speeds. Similarly, at the same train speed, the  $V_{XY}$  curve of R4, without consideration of the vector direction, is almost coincident with that of R1. This further explains that the train-induced flow is symmetrical in the absence of natural wind conditions. In addition, the velocity induced by the tail car passing is less than by the head car passing (Johnson and Holding 2003). In the next section, we will discuss the direction of the induced slipstream effect on the anemometer.

Table 5 Fitting coefficients of slipstream velocities at different train speeds

Coefficients	Head car			Tail car		
	$V_X$	$V_Y$	$V_{XY}$	$V_X$	$V_Y$	$V_{XY}$
$a$	0.0057	0.0113	0.0113	0.0049	0.0097	0.0097
$b$	-0.0067	-0.0133	0	-0.0033	-0.0267	-0.0067

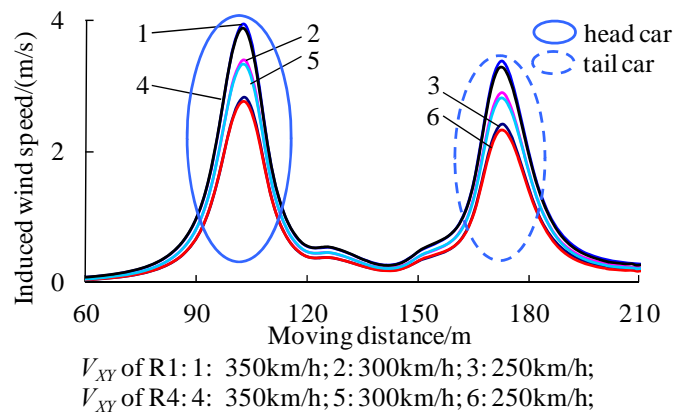
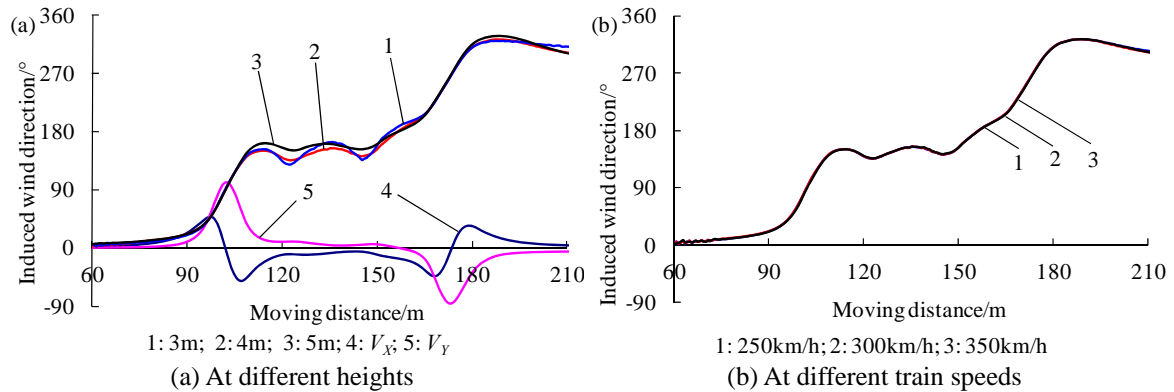


Fig. 9 Contrast analysis of slipstream velocities at points R1 and R4

Fig. 10 Variations of  $V_{XY}$  wind directions

### 3.3.3 Direction of the induced slipstream effect on anemometers

Based on the analysis above, we have obtained the numerical value curves of  $V_{XY}$ , but have not investigated its vector direction. In fact, it is imperative to consider the direction for further study of the train-induced slipstream effect on anemometers. Fig. 10(a) shows the variation of the  $V_{XY}$  wind direction of the induced flow acting on the anemometer under different heights at a train speed of 300 km/h, while Fig. 10(b) presents the variation under different train speeds at the anemometer height of 4 m.

From analyzing the relationship between the wind direction and  $V_Y$  ( $V_X$ ), curve 4 and curve 5 are 30 times the original X component and Y component, respectively. The figures indicate that the variation law of the wind direction is almost the same, irrespective of different anemometer heights or different train speeds. From the head car arriving to the tail car leaving, the wind direction changes about  $330^\circ$ , close to a circle. When the head car is passing at a speed of 300 km/h, the wind direction angle of the speed peak at 4 m height is  $93^\circ$ , while the tail car is  $267^\circ$  (that is  $-93^\circ$ ). Therefore, they are also symmetrical with respect to the trajectory of the center position of the moving train.

## 3.4 Under the case of crosswind

### 3.4.1 Effect of different crosswind speeds

Under the condition without crosswind, it can be concluded that the main effects on the anemometer measurement due to the train-induced slipstream are from both the head car and tail car. However, under crosswinds, which certainly exists along high-speed railways, the environment is changed. Some factors influencing the measurements may be not the same as in the former condition. Thus, it is very important to determine the difference between the two conditions (see Fig. 11), and investigate the peak values of the slipstream effect under different crosswind speeds on the anemometer measurements. The results are shown in Table 6. In this section, the train speed is chosen as 300 km/h, while the height of the anemometer is 4 m. The crosswind speed is set to -12 m/s, -15 m/s, -18 m/s and -20 m/s according to the coordinate system, respectively.

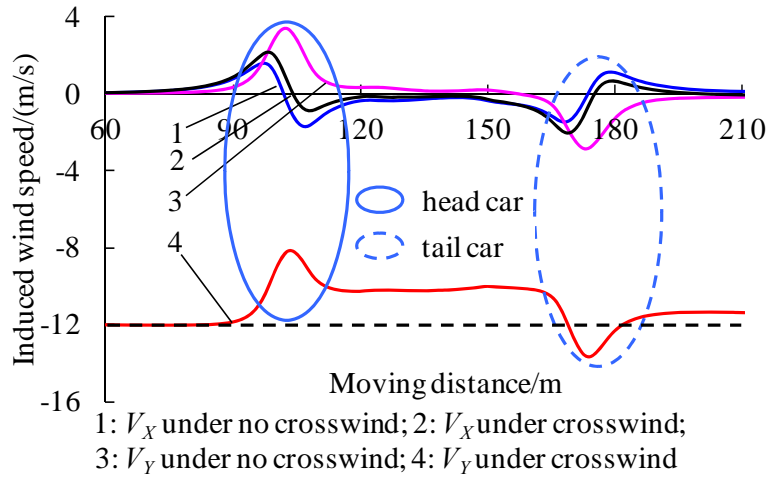


Fig. 11 Comparison of the effect on point R1 under the crosswind and no crosswind conditions

Considering the condition of a -12 m/s crosswind, the law of speed curves due to the train-induced slipstream is the same as that without crosswind. Nevertheless, there is still some difference. Firstly, under crosswind the peak value of  $V_x$  is larger, no matter which car passes the point. Secondly, the absolute value that is the difference between  $V_y$  and  $V_{wind}$  is greater when the head car comes across the point. However, as the tail car is close to it, the value is less than that under the no crosswind condition. Finally, when the middle car passes the point, the absolute value that is the difference between  $V_y$  and  $V_{wind}$  is around 1.85 m/s. This is bigger than that without crosswind, which is near zero. With the crosswind speed increasing, the peaks of  $V_x$ ,  $|V_{XY} - V_{wind}|$  of the head car and the peaks of  $V_x$  of the tail car tend to be greater, while that of  $|V_{XY} - V_{wind}|$  of the tail car just declines. The effect of the induced slipstream owing to the head car on the anemometer strengthens, as it is in line with the crosswind direction. However, that of the tail reduces, as it acts against the crosswind direction. Through the comparison of the specific values, all these show that the crosswind speed has a direct effect on the velocity of the anemometer. The relationship between  $V_{wind}$  and  $V$  ( $V_x$  and  $|V_{XY} - V_{wind}|$ ) can be expressed in linear form and the correlation coefficients are over 0.99. The following formula can be established

$$V_{ij} = aV_{wind} + b$$

where  $j = V_x, |V_{XY} - V_{wind}|$ ,  $i = \text{head car, tail car}$ , and the specific coefficients of  $a, b$  are listed in Table 7.

Fig. 12 is the contrast analysis of induced wind speed at points R1 and R4 with distance at the height of 4 m under a crosswind of 12 m/s, when the train speed is 300 km/h. When the high-speed train passes R1 and R4, there is a large difference between the curves of  $V_x$  at the two monitoring points. The effect of the tail car contributes to making it large. Meanwhile, the curves of  $|V_y|$  and  $V_{XY}$  are almost the same, which shows that  $V_{XY}$  is more dependent on  $V_y$ . In addition, those of R1 are opposite to R4's, and a difference exists when the tail car passes. This indicates that the crosswind and the tail car affect the train-induced flow.

Table 6 Peak values of the slipstream effect under different crosswind speeds

$V_{wind}/$ (m/s)	Head car				Tail car			
	$V_X$ (m/s)	$V_Y$ /(m/s)	$V_{XY}$ /(m/s)	$ V_{XY} - V_{wind} $ (m/s)	$V_X$ /(m/s)	$V_Y$ /(m/s)	$V_{XY}$ /(m/s)	$ V_{XY} - V_{wind} $ (m/s)
-12	2.04	-8.15	8.16	3.84	2.20	-13.67	13.69	1.69
-15	2.18	-10.99	11.00	4.00	2.38	-16.40	16.42	1.42
-18	2.35	-13.83	13.84	4.16	2.58	-19.15	19.17	1.17
-20	2.47	-15.70	15.72	4.28	2.72	-20.99	21.01	1.01
Specific value								
$V_{-15}/V_{-12}$	1.07	-	-	1.04	1.08	-	-	0.84
$V_{-18}/V_{-15}$	1.08	-	-	1.04	1.08	-	-	0.82
$V_{-20}/V_{-18}$	1.05	-	-	1.03	1.05	-	-	0.86

Table 7 Fitting coefficients of slipstream velocities under different crosswind speeds

Coefficients	Head car		Tail car	
	$V_X$	$ V_{XY} - V_{wind} $	$V_X$	$ V_{XY} - V_{wind} $
$a$	0.0539	0.0547	0.065	-0.085
$b$	1.3845	3.1812	1.4132	2.7032

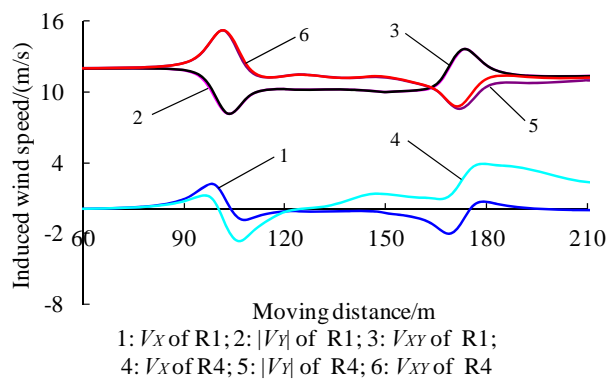


Fig. 12 Contrast analysis of the slipstream speeds at points R1 and R4

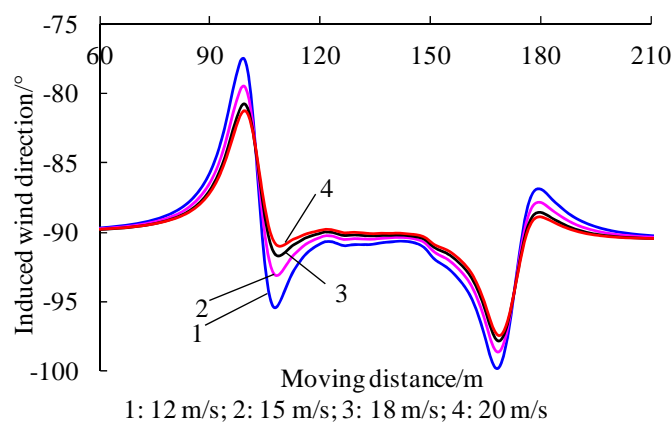


Fig. 13 Variations of wind directions under different crosswind speeds

#### 3.4.2 Direction of the induced slipstream effect on anemometers

In fact, it is imperative to consider the direction for further studying the train-induced slipstream effect on anemometers. Fig. 13 shows the variation of the  $V_{XY}$  wind direction of the induced flow acting on the anemometer under different crosswind speeds.

The figure shows that the variation law of the wind direction is the same, but the peak values are a little different. The less the crosswind speed is, the bigger the peak-to-peak value of induced wind direction is. From the head car arriving to the tail car leaving, the wind direction fluctuates around  $-90^\circ$ . When the head car passes at a speed of 300 km/h, the peak-to-peak value at the wind speed of  $-12$  m/s is larger.

## 4 Conclusions

The dependence of the train-induced slipstream on the height of the anemometer, speed and length of high-speed train, and speed of crosswind have been studied using CFD. The three-dimensional unsteady RANS combined with the eddy viscosity hypothesis were adopted to obtain the horizontal wind speed generated by the head and tail of a passing train. Sliding mesh technology in a commercial CFD software Fluent was utilized to treat the moving boundary problem. The validity of the model developed here is verified with the results of wind tunnel tests in a paper published by Zhang *et al.* (2013). The difference of slipstream between the three-car and eight-car grouping models was analyzed, and shows that using the three-car grouping model to investigate the train-induced flow is reasonable. After that, a series of numerical simulations were carried out to study the influence of the anemometer heights, train speeds, crosswind speeds and the directions of the induced slipstream on the measurements of anemometers.

Based on the results and discuss, the study shows that the influence factors of the train-induced slipstream velocity are the passing head car and tail car, particularly the head, and the length of the train is not very important relatively. With the height of anemometer increasing, the maxima of  $V_x$ ,  $V_y$  and  $V_{xy}$  tend to reduce. The relationship between  $H$  and  $V$  ( $V_x$ ,  $V_y$  and  $V_{xy}$ ) can be expressed in linear form. The train-induced flow field is symmetrical in the absence of natural wind conditions with respect to the trajectory of the center position of the moving train. In addition,  $V_{xy}$  is more

dependent on the  $V_Y$ . With the train speed increasing, the maxima of  $V_X$ ,  $V_Y$  and  $V_{XY}$  enlarge. The relationship between  $V_{\text{train}}$  and  $V$  ( $V_X$ ,  $V_Y$  and  $V_{XY}$ ) can be also expressed with linear increment, which presents a reasonable agreement with the research achievement of Professor Tian in her book, *Train Aerodynamics* (Tian 2007) and the publication by Hassan *et al.* (2010a). From the head car arriving to the tail car leaving, the wind direction changes about  $330^\circ$ , close to a circle. The wind directions of maximum induced air speeds are also symmetrical distribution. Under the case of crosswind, the peak value of  $V_X$  is larger than that of without crosswind. The absolute value that is the difference between  $V_Y$  and  $V_{\text{wind}}$  is greater, when the head car comes across the point. However, as the tail car is close to it, the value is less than that under the no crosswind condition. When the middle car passes the point, the absolute value that is the difference between  $V_Y$  and  $V_{\text{wind}}$  is around 1.85 m/s. This is bigger than that without crosswind, which is near zero. Through the analysis of wind speeds at points R1 and R4, the train-induced flow field is unsymmetrical under crosswind conditions. With the crosswind speed increasing, the peaks of  $V_X$ ,  $|V_{XY} - V_{\text{wind}}|$  of the head car and that of  $V_X$  of the tail car tend to be more, while that of  $|V_{XY} - V_{\text{wind}}|$  of the tail car just declines. The relationship between  $V_{\text{wind}}$  and  $V$  still can be expressed in linear form. Under different crosswind speeds, the less the wind speed is, the bigger the peak-to-peak value of induced wind direction is. From the head car arriving to the tail car leaving, the wind direction angle fluctuates around  $-90^\circ$ .

The results can provide guidance for the measurement and location of anemometers along railway lines, and complement the operational safety management of the train under crosswinds.

## Acknowledgements

The authors acknowledge the computing resources provided by the Institute of High-speed Train of Central South University, China.

The research described in this paper was financially supported by the Scholarship Award for Excellent Innovative Doctoral Student granted by Central South University of China, the National Science Foundation of China (Grant No. 51205418, U1134203 and U1334205).

## References

- Baker, C.J., Sterling, M., Figur-Hardy, G., Johnson, T., Free, P., Munley, G., Bowman, I., Pope, C. and Gawthorpe, R. (2006), "The effect of train slipstreams on passengers and trackside workers", *Proceedings of the 7th world congress on railway research (WCCR)*, Montreal, Canada, June.
- Cali, P.M. and Covert, E.E. (2000), "Experimental measurements of loads on an overhead highway sign structure by vehicle-induced gusts", *J. Wind Eng. Ind. Aerod.*, **84**(1), 87-100.
- Cheli, F., Ripamonti, F., Rocchi, D. and Tomasini, G. (2010), "Aerodynamic behaviour investigation of the new EMUV250 train to cross wind", *J. Wind Eng. Ind. Aerod.*, **98**(2), 189-201.
- Chu, C.R., Chien, S.Y., Wang, C.Y. and Wu, T.R. (2014), "Numerical simulation of two trains intersecting in a tunnel", *Tunn. Undergr. Sp. Tech.*, **42**, 161-174.
- Diedrichs, B., Sima, M., Orellano, A. and Tengstrand, H. (2007), "Crosswind stability of a high-speed train on a high embankment", *Proc. I. Mech. Eng., Part F: J. Rail. Rap. Tran.*, **221**(2), 205-225.
- Fluent Inc. (2006), *FLUENT User's Guide*.
- Fujii, T., Maeda, T., Ishida, H., Imai, T. Tanemoto, K. and Suzuki, M. (1999), "Wind-Induced Accidents of Train/Vehicles and Their Measures in Japan", *QR of RTRI*, **40**(1), 50-55.

- Gong, J. and Wang, P. (2012), "Research on gale monitoring & early warning system of high-speed railway", *High Speed Rail. Tech.*, **3**(1), 5-8, 14. (in Chinese)
- Hemida, H., Gil, N. and Baker, C. (2010), "LES of the slipstream of a rotating train", *J. Fluids Eng.*, **132**(5), 31-39.
- Hemida, H. and Krajnovic, S. (2010), "LES study of the influence of the nose shape and yaw angles on flow structures around trains", *J. Wind Eng. Ind. Aerod.*, **98**(1), 34-46.
- Hemida, H., Baker, C. and Gao G.J. (2014), "The calculation of train slipstreams using large-eddy simulation", *Proc. I. Mech. Eng., Part F: J. Rail. Rap. Tran.*, **228**(1), 25-36.
- Huang, S., Hemida, H. and Yang, M.Z. (2014), "Numerical calculation of the slipstream generated by a CRH2 high-speed train", *Proc. I. Mech. Eng., Part F: J. Rail. Rap. Tran.*, **228**, published online 8 April 2014.
- Hur, N., Kim, S.R., Won, C.S. and Choi, C.K. (2008), "Wind load simulation for high-speed train stations", *J. Wind Eng. Ind. Aerod.*, **96**(11), 2042-2053.
- Johnson, T. and Holding, J. (2003), "Better understanding of high speed train slipstream velocities", *Proceedings of the 6th world congress on railway research (WCCR)*, Edinburgh, UK, September.
- Juraeva, M., Lee J.H. and Song, D.J. (2011), "A computational analysis of the train-wind to identify the best position for the air-curtain installation", *J. Wind Eng. Ind. Aerod.*, **99**(5), 554-559.
- Li, Y.F. and Liang, X.F. (2009), "Aerodynamic function and stability influence of high-speed moving EMUs on insulated boards", *J. Cent. South Univ. (Sci. Tech.)*, **40**(6), 1587-1592. (in Chinese)
- Liu, T.H. and Zhang, J. (2013), "Effect of landform on aerodynamic performance of high-speed trains in cutting under cross wind", *J. Cent. South Univ.*, **20**(3), 830-836.
- Matsumoto, M. and Maeda, T. (1996), "Train/vehicles wind-induced hazard and its mitigation", *Proceedings of the Conference on Natural Disaster Reduction, ASCE*, Washington, D.C., USA, December.
- Quinn, A.D., Baker, C.J. and Wright, N.G. (2001), "Wind and vehicle induced forces on flat plates—Part 1: wind induced force", *J. Wind Eng. Ind. Aerod.*, **89**(9), 817-829.
- Quinn, A.D., Baker, C.J. and Wright, N.G. (2001), "Wind and vehicle induced forces on flat plates—Part 2: vehicle induced force", *J. Wind Eng. Ind. Aerod.*, **89**(9), 831-847.
- Rezvani, M.A. and Mohebbi M. (2014), "Numerical calculations of aerodynamic performance for ATM train at crosswind conditions", *Wind and Struct.*, **18**(5), 529-548.
- Sanz-Andres, A. and Santiago-Prowald, J. (2002), "Train-induced pressure on pedestrians", *J. Wind Eng. Ind. Aerod.*, **90**(8), 1007-1015.
- Sanz-Andres, A., Laveron, A., Cuerva, A. and Baker, C. (2004), "Vehicle-induced force on pedestrians", *J. Wind Eng. Ind. Aerod.*, **92**(2), 185-198.
- Sanz-Andres, A., Laveron, A., Baker, C. and Quinn, A. (2004), "Vehicle induced loads on pedestrian barriers", *J. Wind Eng. Ind. Aerod.*, **92**(5), 413-426.
- Sanz-Andres, A., Santiago-Prowald, J., Baker, C. and Quinn, A. (2003), "Vehicle-induced loads on traffic sign panels", *J. Wind Eng. Ind. Aerod.*, **91**(7), 925-942.
- Shin, C.H. and Park, W.G. (2003), "Numerical study of flow characteristics of the high speed train entering into a tunnel", *Mech. Res. Commun.*, **30**, 287-296.
- Sterling, M., Baker, C.J., Jordan, S.C. and Johnson, T. (2008), "A study of the slipstreams of high-speed passenger trains and freight trains", *Proc. I. Mech. Eng., Part F: J. Rail. Rap. Tran.*, **222**, 177-193.
- Tian, H.Q. (2007), *Train Aerodynamics*, China Railway Press, Beijing, China.
- Wang, B., Xu, Y.L., Zhu, L.D. and Li, Y.L. (2014), "Crosswind effects on high-sided road vehicles with and without movement", *Wind and Struct.*, **18**(2), 155-180.
- Zhang, J., Gao, G.J. and Li, L.J. (2013), "Height optimization of windbreak wall with holes on high-speed railway bridge", *J. Traffic Transport. Eng.*, **13**(6), 28-35. (in Chinese)